

NO-A198 462

GEOMETRIC RESTORATION OF SATELLITE IMAGE DATA(U)

1/1

NORTHWEST RESEARCH ASSOCIATES INC BELLEVUE WA

R D LUCAS ET AL 15 OCT 87 NMRA-CR-R019 AFGL-TR-87-0270

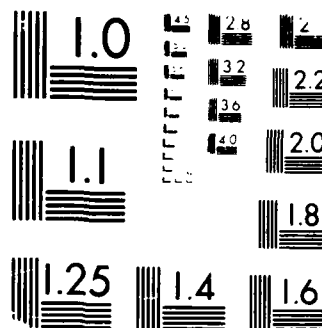
UNCLASSIFIED

F19628-87-C-0003

F/G 8/2

NL





MICROCOPY RESOLUTION TEST CHART  
 NATIONAL BUREAU OF STANDARDS-1963-A

DTIC FILE COPY

(4)

AFGL-TR-87-0270

AD-A190 462

Geometric Restoration of Satellite Image Data

R. David Lucas  
Robert E. Robins

Northwest Research Associates  
P.O. Box 3027  
Bellevue, WA 98009

15 October 1987

Scientific Report No. 3

Approved for public release; distribution unlimited

AIR FORCE GEOPHYSICS LABORATORY  
AIR FORCE SYSTEMS COMMAND  
UNITED STATES AIR FORCE  
HANSCOM AIR FORCE BASE, MASSACHUSETTS 01731

DTIC  
ELECTE  
MAR 02 1988  
S E D

88 2 26 161

This technical report has been reviewed and is approved for publication.

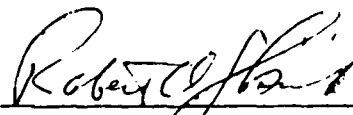


LOIS WLODYKA  
Contract Manager



JOHN E. RASMUSSEN, Chief  
Ionospheric Interactions Branch

FOR THE COMMANDER



ROBERT A. KRIVANEK, Director  
Ionospheric Physics Division

This report has been reviewed by the ESD Public Affairs Office (PA) and is releasable to the National Technical Information Service (NTIS).

Qualified requestors may obtain additional copies from the Defense Technical Information Center. All others should apply to the National Technical Information Service.

If your address has changed, or if you wish to be removed from the mailing list, or if the addressee is no longer employed by your organization, please notify AFGL/DAA, Hanscom AFB, MA 01731. This will assist us in maintaining a current mailing list.

Do not return copies of this report unless contractual obligations or notices on a specific document requires that it be returned.

## REPORT DOCUMENTATION PAGE

1a. REPORT SECURITY CLASSIFICATION Unclassified			1b. RESTRICTIVE MARKINGS <b>A190462</b>	
2a. SECURITY CLASSIFICATION AUTHORITY			3. DISTRIBUTION / AVAILABILITY OF REPORT Approved for public release; distribution unlimited	
2b. DECLASSIFICATION / DOWNGRADING SCHEDULE				
4. PERFORMING ORGANIZATION REPORT NUMBER(S) NWRA-CR-87-R019			5. MONITORING ORGANIZATION REPORT NUMBER(S) AFGL-TR-87-0270	
6a. NAME OF PERFORMING ORGANIZATION Northwest Research Associates	6b. OFFICE SYMBOL (If applicable) CR Division	7a. NAME OF MONITORING ORGANIZATION Air Force Geophysics Laboratory (AFGL)		
6c. ADDRESS (City, State, and ZIP Code) P.O. Box 3027, Bellevue, WA 98009		7b. ADDRESS (City, State, and ZIP Code) Hanscom AFB, MA 01731		
8a. NAME OF FUNDING / SPONSORING ORGANIZATION AFGL	8b. OFFICE SYMBOL (If applicable)	9. PROCUREMENT INSTRUMENT IDENTIFICATION NUMBER F19628-87-C-0003		
8c. ADDRESS (City, State, and ZIP Code) Hanscom AFB, MA 01731		10. SOURCE OF FUNDING NUMBERS		
		PROGRAM ELEMENT NO. 62101F	PROJECT NO. 4643	TASK NO. 08
				WORK UNIT ACCESSION NO. 05
11. TITLE (Include Security Classification) Geometric Restoration of Satellite Image Data				
12. PERSONAL AUTHOR(S) R. David Lucas and Robert E. Robins				
13a. TYPE OF REPORT Scientific No. 3	13b. TIME COVERED FROM 87/2/20 TO 87/9/30	14. DATE OF REPORT (Year, Month, Day) 87/10/15	15. PAGE COUNT 28	
16. SUPPLEMENTARY NOTATION				
17. COSATI CODES			18. SUBJECT TERMS (Continue on reverse if necessary and identify by block number)	
FIELD	GROUP	SUB-GROUP		
			image processing, satellite images, geometric restoration	
19. ABSTRACT (Continue on reverse if necessary and identify by block number) We describe an approach for projecting satellite image data onto arbitrary map coordinates. This transformation removes distortions caused by the basic geometry of cross-track scanners and by spacecraft pitch, roll, and yaw. Geometrically restored images are useful for morphological analyses and correlative studies involving concurrent data from multiple sensors. It is possible, for example, to present AIRS passes from distinct receivers, all-sky camera images, radar data, and other relevant spatial measurements on one map in geographic coordinates. Our approach is rigorous in that arbitrary satellite motions are accounted for and exact principles of geometry are used throughout. The floating-point intensive geometry calculations are performed on an arbitrary (adjustable) reference grid, which can be coarse for quick-look purposes, or fine for highest accuracy. Concurrent images for distinct wavelengths can be efficiently projected without redundant geometry calculations. An IBM PC/AT compatible implementation for Polar BEAR AIRS image data is described. Results are presented for two data sets representing moderate and severe platform motions.				
20. DISTRIBUTION / AVAILABILITY OF ABSTRACT <input type="checkbox"/> UNCLASSIFIED/UNLIMITED <input type="checkbox"/> SAME AS RPT <input type="checkbox"/> DTIC USERS			21. ABSTRACT SECURITY CLASSIFICATION Unclassified	
22a. NAME OF RESPONSIBLE INDIVIDUAL Lois Wlodyka			22b. TELEPHONE (Include Area Code)	22c. OFFICE SYMBOL AFGL/LID

# Table of Contents

	<u>Page</u>
DD Form 1473	
1. Introduction	1
2. Approach	3
3. Results	11
4. Conclusions	19
References	20
Plates	

Accession For	
NTIS GRA&I	<input checked="" type="checkbox"/>
DTIC TAB	<input type="checkbox"/>
Unannounced	<input type="checkbox"/>
Justification	
By	
Distribution/	
Availability Codes	
Avail and/or	
Dist	Special
A-1	



## 1 Introduction

Images are two-dimensional projections of three-dimensional objects. Just as a navigator cannot use maps without knowing their projection properties, the interpretation of remotely sensed areal data must take into account the geometry associated with the sampling system. Geometrical restoration is the rational projection of image data onto canonical map coordinates. We do this so that the morphological aspects of the observed phenomena can be interpreted more readily in geophysical terms.

The geometrical distortions inherent with satellite scanning systems are well known. For AIM or AIRS, when the spacecraft is oriented nominally, the viewing geometry is bilaterally symmetric and the sample spot on the ionosphere varies from about 5 x 20 km at nadir to about 60 x 90 km near the limb. In a raw image, obtained by mapping samples directly to pixels, cross-track scales will be nonuniform, the distortion increasing progressively from the nadir toward the limb; ionospheric features that are square near the nadir will show vanishing lateral dimensions near the limb. In practice, the problem is greatly complicated by unsteady motions of the platform. Pitch, roll, and yaw excursions with time scales from seconds to hours and occasionally with large amplitudes can produce images that are impossible to interpret in raw form.

Fortunately in the case of the Polar BEAR satellite, appropriate orientation data are usually available, at least when the spacecraft is in sunlight, such that instantaneous attitude can be estimated. In theory, if we know the position and orientation of the scanning mirror at any time, we can compute where the ray of observation intercepts an ionospheric surface. If we have some way of interpolating in two dimensions, the set of discrete samples can be transformed into an image rendered on an appropriate geographic projection.

This report describes an implementation of these ideas. The basic approach has been adapted from our work on the processing of all-sky camera images [1]. Although ground-based cameras and satellite-borne scanners present distinct geometrical problems, the same basic approach can be applied in both cases.

For the geometrical restoration of AIRS image data, our approach offers the following features:

**Arbitrary satellite motion.** We make no small-amplitude assumptions regarding the motion of the platform. We do, however, assume that the motion is known, *i.e.*, that we have reliable time-series data for pitch, roll, yaw, altitude, latitude, and longitude. We also assume that the motions are resolved, which

means that the motion time scales should be long compared with the mirror scan time, 3 seconds, and the navigation data sample interval.

**Exact geometrical principles.** We make no "flat-earth" assumptions. The emitting surface is assumed to be an earth-centered sphere of arbitrary radius.

**Arbitrary map projection.** We generally produce geometrically restored images on geographic polar coordinates, although any other definable map projection could be adopted. This feature makes it easy to overlay multiple images. For example, AIRS images captured from multiple receiver sites and concurrent all-sky camera images could be combined on one polar cap-scale map.

**User-selectable accuracy/speed.** Geometrical computations are floating-point intensive. On a small computer, it takes on the order of an hour to calculate the projection of all samples (typically  $326 \times 200$ ) into the display domain. The user can define a coarse grid (say  $50 \times 50$ ) for the calculation of exact projection geometry. Actual projections are computed by bilinear interpolation on this grid. This affords an optional quick look at an approximately restored image. Note that the full resolution of the image data is always preserved. The coarse grid is used only to compute the projection of each sample to the display raster.

Our approach, indeed any approach to the geometrical restoration of these data, is subject to a variety of fundamental limitations. First, we assume that the observed emissions come from a single ionospheric layer; hence, three-dimensional structures will not be accurately projected. Second, the data are collected over both space and time, and the relative contributions of temporal and spatial variability in the observed phenomena are unknown. Third, inaccuracies in the navigation data, particularly platform attitude, may produce large errors. This is particularly true near the limb, where small errors in pitch, roll, or yaw will produce large errors in the restored image. Fourth, gaps in the attitude data, such as during spacecraft night, will stop the restoration processing, unless some method of estimating night-side attitude is available. Finally, in some circumstances the phenomena of interest may be under-sampled. This problem, most commonly manifested near the limb, has two sources: (1) the sample spot becomes relatively large near the limb, and consequent nonuniform resolution may bias the interpretation of the image; and (2) attitude variations, particularly yaw, may become sufficiently vigorous that consecutive scans do not overlap, leaving areal gaps in the record.

This discussion will focus on geometrical restoration. We will not consider photometric issues associated with AIRS image data. We will not, for example, be concerned with the calibration of the intensity data. Rosenberg's investigation [2] of the AIRS image data has placed greater emphasis on photometric issues, while adopting a less rigorous approach to the geometric restoration problem. Physical interpretations of the data are also outside the scope of this report.



## 2 Approach

In raw form, the Polar BEAR data stream consists of a mixture of data from several instruments and housekeeping functions. Batch-mode processing of these data produces a variety of data products. For our purposes, the data from a single receiver pass can be reduced to five files: four image files corresponding to distinct wavelengths, and one file representing a navigation data time series. Image files consist of a variable-length header followed by  $326 \times N$  8-bit samples, where  $N$  is the number, typically about 250, of mirror scans captured in the pass. The navigation data is in the form of a table of time, altitude, latitude, longitude, pitch, roll, and yaw. The temporal resolution of the navigation data is arbitrary, 15 seconds being typical. (The minimum sample interval is .5 seconds, the telemetry frame time.)

We want to project the observed image data onto a specific map. This image will be rendered on a display raster consisting of  $M \times N$  pixels. Hence, once the *desired map and viewport are defined*, there exists a relationship between the address of a pixel and the position (e.g. latitude and longitude) of that pixel in world coordinates. In this report,  $x$  and  $y$  ( $X$  and  $Y$ ) are Cartesian coordinates defined on the sample (display) domains. The origin is the upper-left corner, coincident with the first sample (pixel). The sample (display) set, denoted by  $i$  and  $j$  ( $I$  and  $J$ ) are the vertices of a finite two-dimensional grid corresponding to integer values of  $x$  and  $y$  ( $X$  and  $Y$ ).

The situation is depicted in Figure 1. The heavy grid is defined on the sample domain ( $xy$ ). Each vertex ( $ij$ ) corresponds to an AIRS imager sample. (We sketch a hypothetical  $5 \times 5$  sample domain. The real grid is obviously much larger.) The light grid represents the display raster projected onto the sample domain.

The geometrical restoration problem would be relatively straightforward (and it is in the case of all-sky camera images) if we could project directly from the display domain to the sample domain. As shown in Figure 1, those pixels that fall within the sample set then would be assigned intensities by simple interpolation. (Bilinear interpolation will generally suffice, although higher-order methods could be implemented. When speed is particularly important, nearest-neighbor resampling may be selected.) Unfortunately, the nonlinear nature of the projection geometry and its dependence on tabulated navigation data make it impossible to compute  $(x,y)$  directly from  $(X,Y)$ . Given a point on the ionosphere, there is no direct method that will determine the instant in time when the scanning mirror looks in that direction.

We can always compute directly from  $(x,y)$  to  $(X,Y)$ . This calculation is shown schematically in Figure 2. We start with  $s(x,y)$ , which denotes a Cartesian position on the sample domain. For any  $(x,y)$ , we compute the time relative to the first sample.

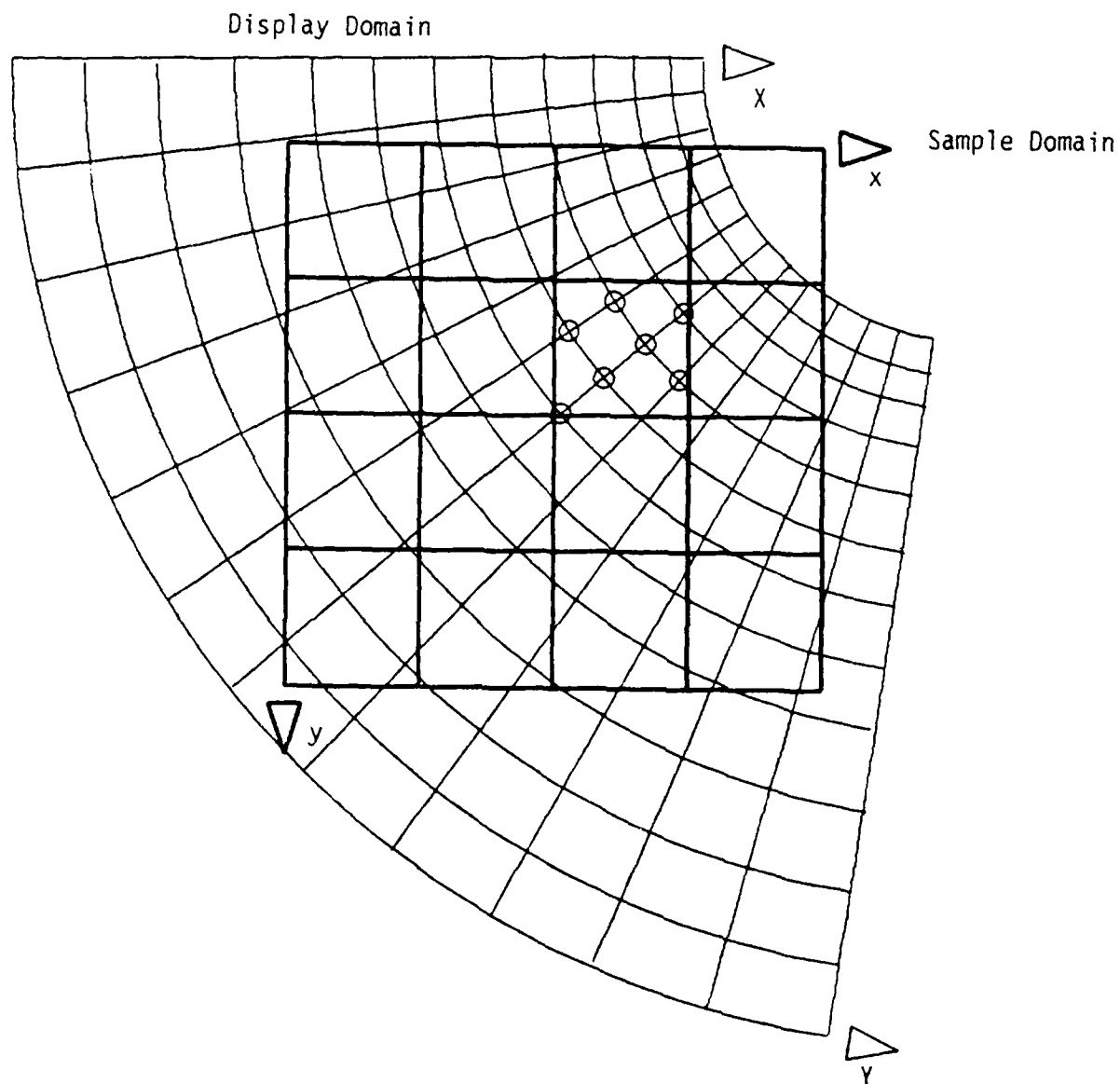


Figure 1. The heavy grid represents the sample set defined on the sample domain,  $xy$ . The lighter grid represents the display set which has been projected onto the sample domain. The circles enclose display pixels that map into a specific sample cell. Their intensities are estimated by bilinear interpolation within that cell.

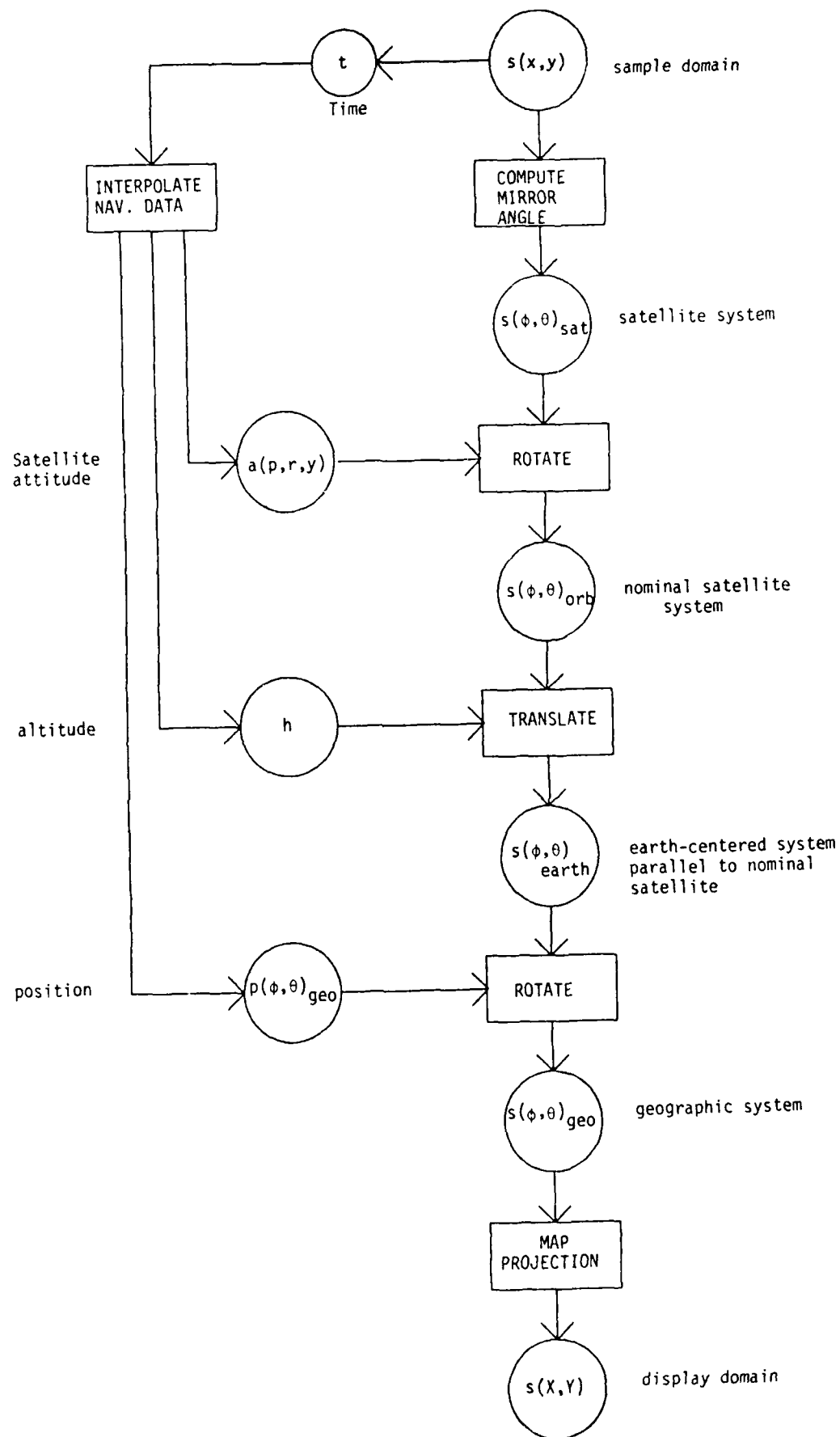


Figure 2. Flow chart for the computation of the position,  $s(X,Y)$ , on the display domain of a position on the sample domain,  $s(x,y)$ .

$$\text{time} = 3(y + x/325),$$

and the mirror angle, relative to nadir,

$$\text{mirror angle} = 134.4(x - 325./2)/325.$$

Note that although the sample set is discrete, the above expressions can be applied for real  $x$  and  $y$ , producing fictitious mirror angles and times corresponding to positions on a continuous sample domain. The time value is used to interpolate in the navigation data to obtain an instantaneous attitude (pitch, roll, yaw), altitude, and position. The latter, denoted  $p(\phi, \theta)_{\text{geo}}$ , is expressed in an appropriate earth-fixed spherical coordinate system. The mirror angle is expressed in a satellite-fixed spherical system,  $s(\phi, \theta)_{\text{sat}}$ . The attitude angles are used to rotate to a nominal satellite system, i.e. pitch = roll = yaw = 0. The altitude is used to translate to a parallel system centered in the earth,  $s(\phi, \theta)_{\text{earth}}$ . This step requires that the altitude of the source be known. We might, for example, assume that the observed emissions came from the E region at 110 km. The spacecraft's position then is used to rotate to geographic coordinates,  $s(\phi, \theta)_{\text{geo}}$ . Finally, these are converted to display domain coordinates,  $s(X, Y)$ , according to a specific map projection.

Note that exact geometrical principles are used throughout the above sequence of computations. The matrix operations used for coordinate system rotations and translations are described in standard texts, e.g. [3].

In our approach, the calculations outlined above are used to project from  $(x, y)$  to  $(X, Y)$ , and two-dimensional interpolation is then used to transform from  $(X, Y)$  back to  $(x, y)$ . The idea is demonstrated in Figure 3 for an analogous one-dimensional sampling problem. The tic marks on the  $x$  axis represent the raw sample points. The curve  $z(i)$  is the vector of samples. A set of reference positions  $\{x'\}$  is selected, and positions in the display domain,  $X(x')$ , are computed (step 1, as numbered in Figure 3). In general, the reference positions do not correspond to display positions, which are denoted by tic marks on the  $X$  axis. For each pair of adjacent  $x'$  values, all bracketed display positions,  $l$ , are located, and their corresponding sample domain positions,  $x_l$ , then are estimated by linear interpolation on the  $X(x')$  curve (step 2). The  $x_l$  then are used to compute  $Z(l)$  by linear interpolation in the  $z(i)$  data (step 3).

Note that two independent resampling steps are involved in this process. One involves the geometrical relationship between the sample and display domains, and the other is the interpolation of intensity on the sample set. The resolutions used in each resampling step are decoupled, and the full resolution of the data is always used in the intensity resampling.

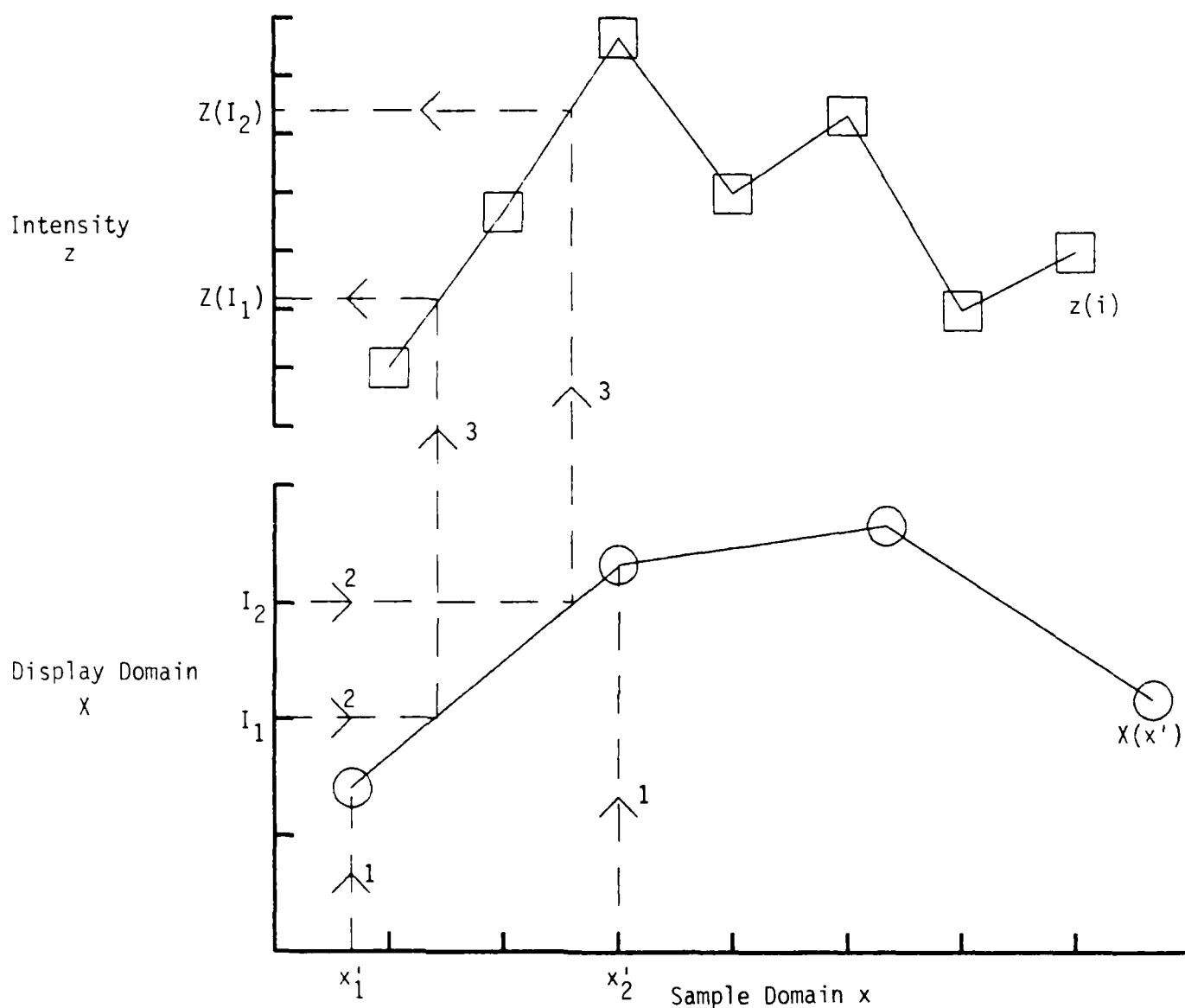


Figure 3. One-dimensional analog of the projection of data from the sample domain to the display domain and back. Tic marks on the x axis represent the sample set. The positions of  $x'$  represent the reference set. The goal is to estimate the set,  $Z(I)$ , of intensities from the given image data,  $z(i)$ . The dashed lines represent the calculation sequence with numbered steps as described in the text.

In the generalization of this idea to two dimensions, piecewise linear curves become surfaces comprised of triangular elements. This is depicted in Figure 4. The upper grid (a) is defined in the sample domain. Both the sample grid and the lower resolution reference grid are shown. (The reference set shown here represents a four-to-one decimation of the sample set, but this is merely a special case. The reference set is arbitrary and, in general, does not correspond to an integer subset of  $x$  and  $y$ .) Diagonal lines drawn across each cell in the reference grid create a set of triangular elements. One of these, identified by the three circle-enclosed vertices, is shown in (b) projected onto the display domain,  $XY$  (step 1). The square-enclosed vertices are the pixels contained by the selected triangular element. The position  $(x,y)$  on the sample domain of each of these pixels can be found by a pair of bilinear interpolations, one each for  $x$  and  $y$  (step 2). The result is shown in (c).

By systematically visiting each triangular element and performing the above calculations for each enclosed pixel, we can generate a table with the following columns:

$$I, J, i, j, r, s$$

where  $(I,J)$  identifies a display pixel address,  $(i,j)$  is the sample grid cell to which that pixel maps, and  $(r,s)$  denotes the fractional offsets within that cell, i.e.,  $x = i + r$ , and  $y = j + s$ , with  $r$  and  $s$  defined on  $(0, 1)$ . This table can be used to project the image data onto the display raster (step 3). Each entry in the table identifies the target pixel,  $(I,J)$ , and the source data cell,  $(i,j)$ . For nearest-neighbor resampling,

$$Z(I,J) = z([i],[j]),$$

where  $[i] = \text{integer}(i + r + .5)$  and  $[j] = \text{integer}(j + s + .5)$ . Alternatively, the following expression yields the bilinear interpolant:

$$\begin{aligned} Z(I,J) = & z(i,j) + r (z(i+1,j) - z(i,j)) + s (z(i,j+1) - z(i,j)) \\ & + r s (z(i,j) + z(i+1,j+1) - z(i+1,j) - z(i,j+1)). \end{aligned}$$

The choice of interpolation scheme will depend on whether the user, in a given instance, wants speed or accuracy.

For maximum efficiency, the interpolation table is sorted on  $(i,j)$ , which is consistent with the order of the raw image data. Then the image and interpolation data files can be processed sequentially in parallel. In the case of bilinear interpolation, the  $z$ -dependent factors can be fetched once for the calculation of all  $Z(I,J)$  contained in a given cell.

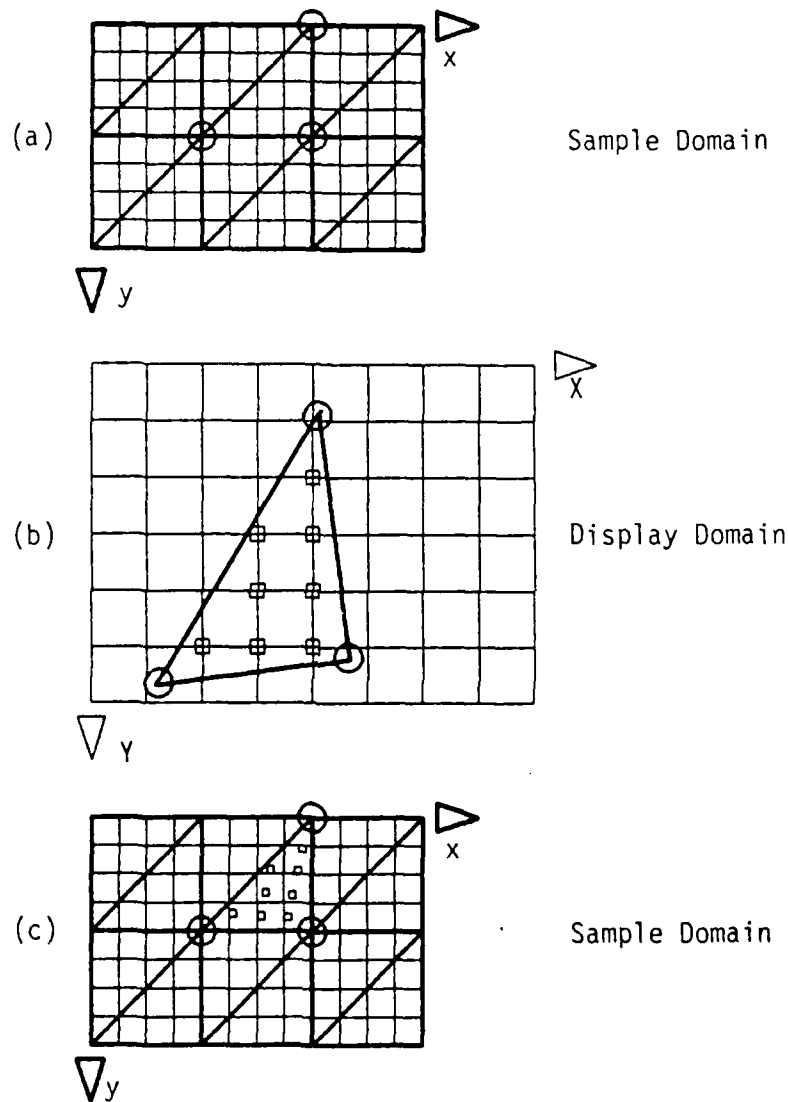


Figure 4. The projection of two-dimensional data from the sample to the display domain and back. In (a) the light grid represents the sample set, and the heavy grid represents the reference set. Diagonal lines divide this grid into a set of triangular interpolation elements. One of these elements is shown in (b) projected onto the display domain. The squares denote those pixels within the image of that element. Bilinear interpolation is used to project these positions back to the sample domain, producing the configuration shown in (c).

The decoupling of the reference set from the sample set is an important feature of our approach. It is often useful, for example, to define a 10 x 10 reference set. For a 256 x 240 output window, the geometric restoration processing in this case will take on the order of one minute and provides reasonable accuracy except, perhaps, near the edges of the image. When a more accurate result is required, say in the preparation of an image for presentation or publication, a finer reference grid should be defined. We used a 50 x 50 reference grid for the results presented in this report. For a 512 x 480 output image, the calculation of the interpolation tables took approximately 17 minutes each.

The interpolation table can be used to control the projection of multiple images. Typically at least three of the images in a given pass will be projected to a single ionospheric altitude. After the interpolation table has been computed, all three images can be projected quickly to the display raster. This avoids wasteful recalculation of redundant geometry results. The projection processing from a pre-computed interpolation table typically takes on the order of one minute.

The approach described above has been implemented in C-language code running on an IBM PC-AT under MS-DOS. This system includes an 8 MHz math coprocessor (Intel 80287), 2 Mbytes of expanded memory, and a 512<sup>2</sup> x 12 frame buffer (Imaging Technology, Inc., FG-100-AT).



### 3 Results

We will illustrate geometric restoration processing for two AIRS passes, representing cases of moderate and severe platform motions. Polar BEAR pass PB1866 (NWRA processing designation) occurred on Day 47, 1987, at Greenwich Time (GT) 18:58. Pass PB2045 occurred on Day 82, 1987, at GT 0630. The data for these two passes were recorded by the transportable HiLat/P.BEAR receiver, Rover, stationed at Poker Flat, Alaska.

The satellite attitude and position time series for these passes are presented in Tables 1 and 2, and the attitude data are plotted in Figure 5. (Sign conventions are as follows: positive pitch is "nose" down, positive roll is left "wing" up, and positive yaw is "nose" left. These angles must be applied in the sequence: pitch, then roll, then yaw.) For PB1866, the amplitudes of the pitch, roll, and yaw motions are approximately 2, 3, and 20 degrees, respectively. For PB2045, these amplitudes are 22, 31, and 156 degrees. In both cases, the roll and yaw motions are approximately periodic over 5-7 minutes, with yaw leading yaw roll about 90 degrees in phase. Pitch is approximately 180 degrees out of phase with yaw and includes a long-term component, which appears as a trend over the span of these data. In both passes, the roll motion includes a 2-3 degree negative offset. We note in passing that the yaw-roll phase relationship observed in these data is consistent with a simple precessing-gyroscope dynamic model. This model suggests a particular relationship between the direction of rotation of the Polar BEAR momentum wheel and the sign of the yaw-roll phase difference. The apparent consistency of the data with this model constitutes evidence that our coordinate system definitions and pitch-roll-yaw sign conventions are in in order.

Plates 1 and 2 show the raw 3914 A images for these two passes. These are derived from the "packed" samples, which are approximately proportional to the logarithm of intensity. In these images, the scan direction is horizontal and time increases downward. The color scale maps low intensities to purple and high intensities to red. (The horizontal line near the bottom of the PB1866 image is a processing artifact caused by an error in our image-data stripping code. This error has since been corrected, and its effect in the images presented here should be ignored.)

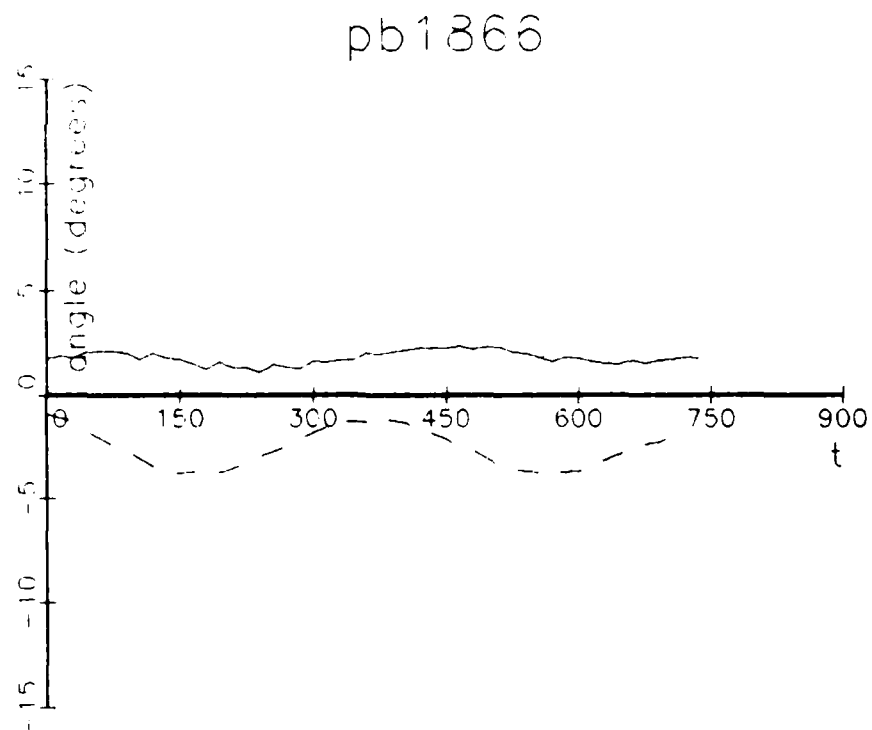
The red and yellow striped band in both images is the day-night terminator, with darkness on the left. The banding in the vicinity of the terminator apparently represents counter overflows. When the intensity exceeds a certain threshold, the receptor automatically switches to a low-sensitivity mode, causing the abrupt transition from high (yellow-red) to low counts (purple-blue) as the scanner crosses the terminator into daylight. Optical emissions are detected on the day side with the scanner in this low-sensitivity mode, with some limb-brightening apparent near the right edge of these images. A low-inten-

Table 1. Position and attitude time series for PB1866. Time is seconds relative to first image sample. Altitude is in kilometers. Geographic position and attitude angles are in degrees.

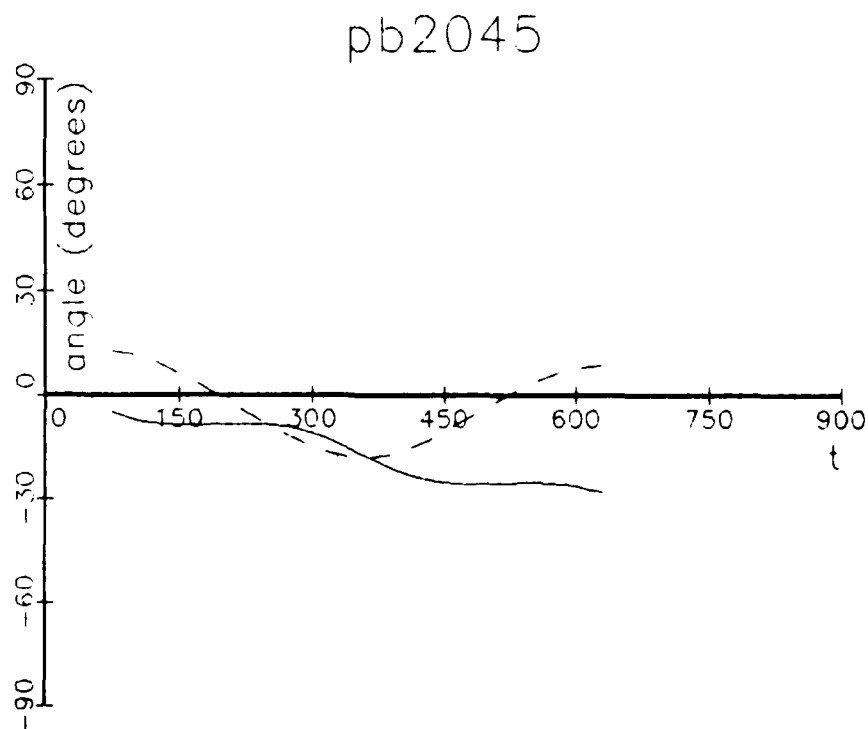
TIME	ALT	LAT	LON	PITCH	ROLL	YAW
0.000	1020.115	83.991	48.459	1.795	-0.906	-6.722
15.000	1020.469	84.838	49.088	1.899	-1.100	-8.738
30.000	1020.821	85.684	49.988	1.827	-1.239	-10.115
45.000	1021.173	86.528	51.356	2.077	-1.741	-10.584
60.000	1021.523	87.368	53.638	2.102	-2.083	-10.616
75.000	1021.872	88.200	58.100	2.136	-2.395	-10.660
90.000	1022.219	89.002	70.040	2.023	-2.774	-9.063
105.000	1022.565	89.558	127.797	1.736	-2.909	-7.661
120.000	1022.909	89.085	-164.930	2.032	-3.443	-5.659
135.000	1023.252	88.291	-151.185	1.765	-3.624	-2.911
150.000	1023.592	87.461	-146.312	1.699	-3.824	-0.346
165.000	1023.932	86.621	-143.879	1.471	-3.707	1.452
180.000	1024.269	85.778	-142.440	1.217	-3.645	4.351
195.000	1024.604	84.933	-141.501	1.576	-3.815	6.156
210.000	1024.937	84.087	-140.848	1.355	-3.527	7.959
225.000	1025.268	83.240	-140.373	1.331	-3.318	9.092
240.000	1025.597	82.393	-140.018	1.097	-2.942	10.600
255.000	1025.924	81.546	-139.746	1.495	-2.881	10.388
270.000	1026.249	80.698	-139.535	1.356	-2.429	9.857
285.000	1026.570	79.850	-139.369	1.272	-2.021	8.693
300.000	1026.890	79.002	-139.238	1.641	-1.918	7.253
315.000	1027.206	78.154	-139.134	1.580	-1.548	5.314
330.000	1027.521	77.306	-139.052	1.683	-1.368	3.328
345.000	1027.832	76.458	-138.989	1.688	-1.161	1.222
360.000	1028.141	75.610	-138.939	2.040	-1.276	-1.331
375.000	1028.447	74.762	-138.902	1.975	-1.158	-3.428
390.000	1028.749	73.913	-138.876	2.077	-1.220	-5.447
405.000	1029.049	73.065	-138.858	2.161	-1.353	-7.325
420.000	1029.346	72.217	-138.847	2.257	-1.600	-8.288
435.000	1029.639	71.368	-138.843	2.287	-1.869	-9.381
450.000	1029.929	70.519	-138.845	2.245	-2.104	-9.492
465.000	1030.216	69.671	-138.851	2.362	-2.495	-9.226
480.000	1030.500	68.823	-138.862	2.210	-2.670	-8.146
495.000	1030.780	67.974	-138.877	2.333	-3.078	-7.091
510.000	1031.056	67.125	-138.895	2.292	-3.375	-5.284
525.000	1031.329	66.276	-138.916	2.062	-3.520	-3.171
540.000	1031.598	65.427	-138.939	2.040	-3.757	-1.332
555.000	1031.863	64.579	-138.966	1.832	-3.730	1.141
570.000	1032.124	63.729	-138.994	1.615	-3.643	3.335
585.000	1032.382	62.880	-139.024	1.811	-3.767	4.952
600.000	1032.635	62.031	-139.056	1.793	-3.692	6.271
615.000	1032.885	61.182	-139.090	1.636	-3.418	7.388
630.000	1033.130	60.333	-139.126	1.531	-3.098	8.954
645.000	1033.370	59.483	-139.162	1.499	-2.835	9.043
660.000	1033.607	58.634	-139.200	1.661	-2.702	8.511
675.000	1033.839	57.784	-139.240	1.521	-2.355	7.537
690.000	1034.067	56.934	-139.280	1.696	-2.251	6.141
705.000	1034.290	56.085	-139.321	1.701	-2.034	4.857
720.000	1034.509	55.235	-139.363	1.811	-1.926	3.285
735.000	1034.723	54.385	-139.406	1.751	-1.711	1.372

Table 2. Position and attitude time series for PB2045. Time is seconds relative to first image sample. Altitude is in kilometers. Geographic position and attitude angles are in degrees.

TIME	ALT	LAT	LON	PITCH	ROLL	YAW
75.000	1031.816	58.986	-163.863	-4.903	12.713	-36.187
90.000	1031.576	59.836	-163.900	-6.280	12.116	-46.266
105.000	1031.333	60.686	-163.936	-7.359	11.489	-54.863
120.000	1031.086	61.535	-163.971	-7.966	10.046	-62.978
135.000	1030.834	62.385	-164.004	-8.392	8.452	-69.348
150.000	1030.580	63.235	-164.036	-8.576	6.416	-74.491
165.000	1030.321	64.084	-164.065	-8.589	4.335	-77.696
180.000	1030.060	64.933	-164.093	-8.622	2.295	-80.189
195.000	1029.794	65.783	-164.118	-8.437	-0.086	-80.390
210.000	1029.525	66.632	-164.140	-8.315	-2.392	-79.574
225.000	1029.253	67.481	-164.160	-8.259	-4.595	-77.250
240.000	1028.978	68.330	-164.177	-8.297	-6.918	-73.049
255.000	1028.700	69.179	-164.190	-8.570	-8.969	-67.337
270.000	1028.416	70.034	-164.199	-8.965	-11.283	-60.097
285.000	1028.134	70.877	-164.203	-9.898	-12.912	-50.955
300.000	1027.846	71.726	-164.202	-10.994	-14.702	-40.560
315.000	1027.556	72.575	-164.196	-12.248	-16.119	-29.613
330.000	1027.262	73.424	-164.182	-13.976	-17.207	-16.675
345.000	1026.966	74.273	-164.160	-15.651	-17.704	-4.427
360.000	1026.668	75.121	-164.129	-17.344	-18.092	8.163
375.000	1026.367	75.970	-164.087	-19.203	-17.819	20.983
390.000	1026.063	76.818	-164.032	-20.905	-17.083	32.979
405.000	1025.758	77.666	-163.961	-22.443	-15.814	44.083
420.000	1025.449	78.515	-163.870	-23.503	-14.498	53.193
435.000	1025.138	79.364	-163.755	-24.410	-12.577	60.805
450.000	1024.826	80.211	-163.610	-25.056	-10.477	67.523
465.000	1024.511	81.060	-163.426	-25.371	-8.358	71.458
480.000	1024.194	81.907	-163.191	-25.430	-6.297	74.197
495.000	1023.875	82.756	-162.886	-25.416	-4.087	75.042
510.000	1023.555	83.602	-162.485	-25.335	-1.790	74.280
525.000	1023.232	84.450	-161.942	-25.142	0.254	71.985
540.000	1022.908	85.295	-161.183	-25.115	2.246	67.465
555.000	1022.582	86.141	-160.064	-25.091	4.137	61.952
570.000	1022.254	86.983	-158.285	-25.255	5.654	54.345
585.000	1021.925	87.819	-155.092	-25.507	6.909	45.381
600.000	1021.595	88.640	-147.912	-25.896	7.827	35.645
615.000	1021.263	89.380	-121.667	-27.027	8.017	24.371
630.000	1020.930	89.397	-33.729	-27.593	8.602	15.150



(a)



(b)

Figure 5. Attitude angles for two Polar BEAR passes: PB1866 in (a) and PB2045 in (b). The solid, dashed, and dotted lines are pitch, roll, and yaw, respectively. Time is seconds relative to the first image datum.

sity (purple) band is visible near the right edge of both images, particularly in Plate 1 for PB1866. The left edge of this band is the horizon, a discontinuity between the limb on the left and black space on the right. At the right edge, the scanner apparently switched back to normal sensitivity, producing a sudden transition from purple to yellow.

Both raw images reveal satellite motion-induced effects. In Plate 1, the "S" shape of the terminator and the sinusoidal shape of the limb are produced by the combined influence of yaw and roll. The more energetic motion in PB2045 produces the chaotic terminator and limb geometries seen in Plate 2.

Plates 3 and 4 show the results of geometric restoration processing for measured position data (latitude, longitude, and altitude) and nominal attitude data, *i.e.* with pitch, roll, yaw angles assumed to be zero. The data are projected onto a polar map of a 110-km ionosphere, with underlying land and water in grays and an overlaid latitude and longitude grid. This processing compensated for distortions arising from the nominal scanning geometry and from earth-curvature and map-projection effects. PB2045 was an ascending pass, and the appropriate "mirror reversal", relative to the raw image, is seen in Plate 4. Motion-induced effects are still apparent, however, producing the sinusoidal shapes in Plate 3 and the scrambled appearance of the PB2045 image in Plate 4.

One effect of geometric restoration is a stretching near the limb. In Plate 3, we see that this amplifies an apparent high-frequency motion effect, giving the limb a pronounced "saw-tooth" form. With close examination, this effect can be seen also in the raw data. It is caused by a 25-30 second component in the Polar BEAR motion spectrum. Figure 6 shows the magnetometer and sun-sensor data for PB1866. These data, together with a geomagnetic field model, are processed by the attitude-estimation code to produce the data shown in Figure 5a. The B2 magnetic-field component clearly shows both the 5-7 minute and 25-30 second components. These are also apparent in the sun-sensor data, but the high-frequency component is "jerky", perhaps because of sampling limitations of the solar direction sensor.

Unaware of the high-frequency (25-30 second period) motion effects when we began our processing of the AIRS images, we used 15-second navigation data to drive the geometrical restoration processing. These data clearly are inadequate for compensating the high-frequency motion effects. Fortunately, our codes are written to accept arbitrarily sampled navigation data, and it would be straightforward to use high-frequency attitude data, with a sample interval less than 5 seconds, say. Whether this would successfully remove the high-frequency motion contamination is problematical, however, since, as we saw in Figure 6b, there are reasons to doubt the accuracy of the attitude source data at these frequencies.

Plates 5 and 6 show the results of geometric restoration using the full navigation time series (Tables 1 and 2). In Plate 5, for PB1866, we see a continuously curved terminator and a nearly linear

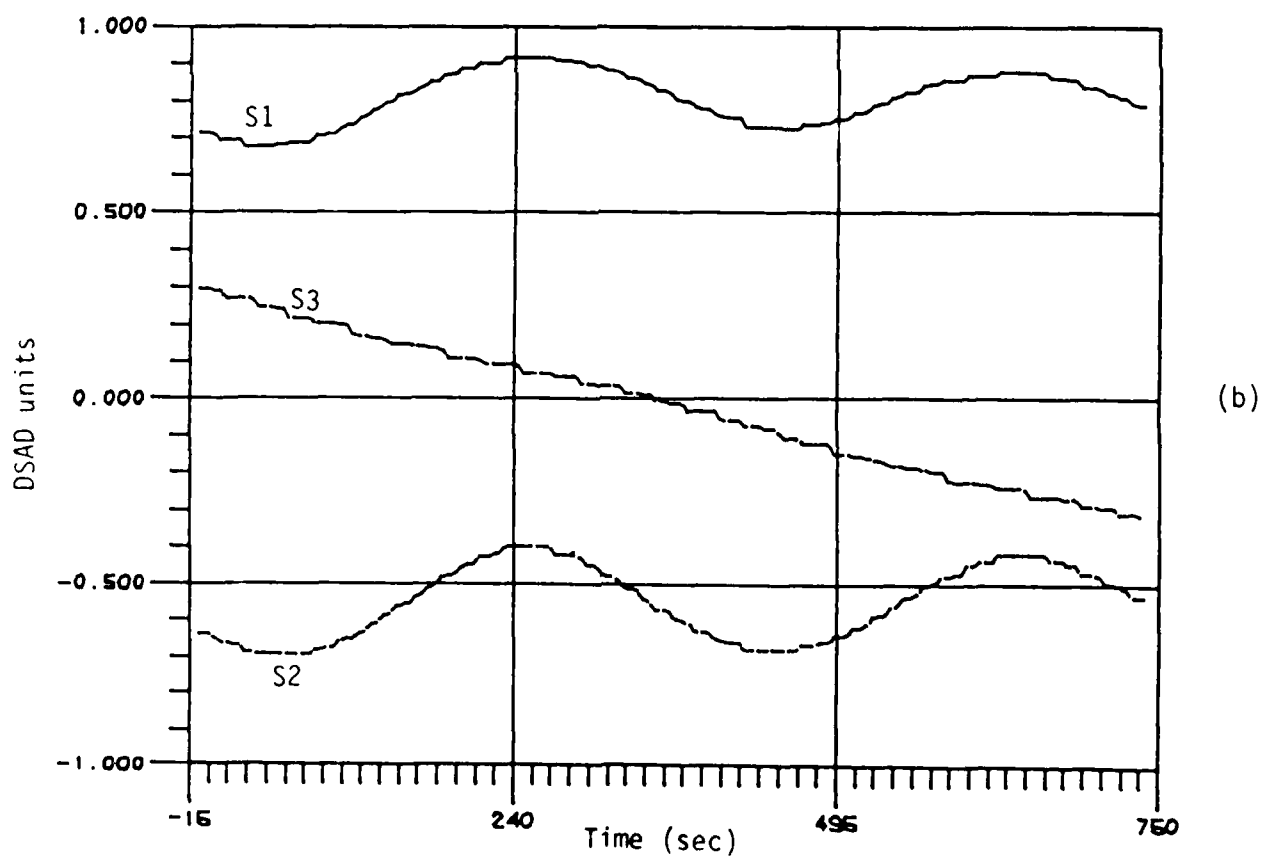
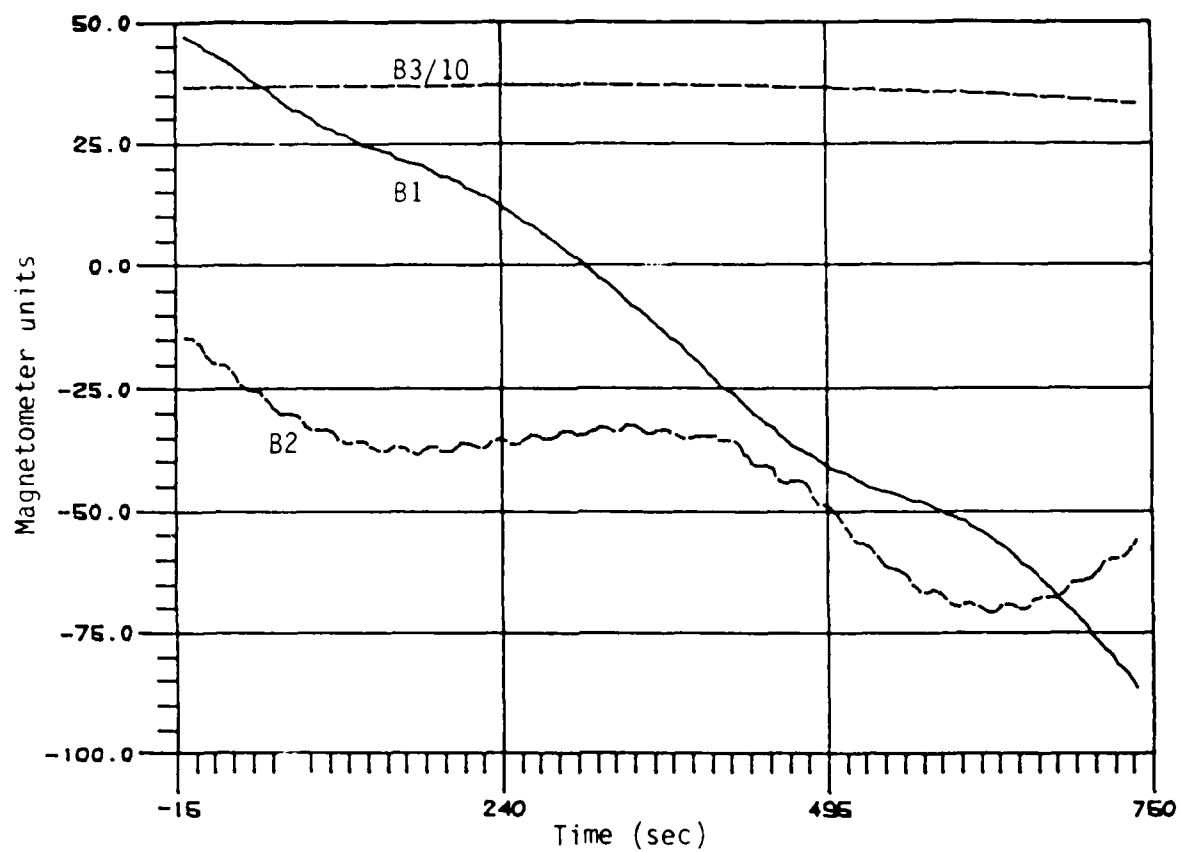


Figure 6. Magnetometer (a) and sun-sensor (b) data for PB1866. A 5-second sample rate has been used for these data.

limb, both largely free of the motion contamination so apparent in Plates 1 and 3. (The high-frequency motion effects, of course, are still present.)

Comparison of the raw (Plate 1) and restored (Plate 5) images reveals that the geometric processing clips the data. This is necessary because the scanner field of view near the extremes of mirror travel often does not intercept the assumed ionosphere (110 km), and the data gathered there cannot be projected onto the display map. In PB1866, the data at the left end of all scans have been clipped, and all right ends have been clipped except for two regions, appearing as triangular cutouts in Plate 5. These cutouts coincide with two roll angle minima (see Figure 5a) where the satellite was tilted strongly to the west. The shapes of these cutouts reflect the pronounced influence of roll motions on the projection of data near the limb.

If the apparent horizon were at 110-km tangent altitude, PB1866 image data on the right, beyond and including the purple band, would be above the limb and would be clipped in the restored image. This is not the case, however, possibly indicating that the apparent horizon is at substantially lower altitudes, or that the attitude data is biased in some way. A brief examination of these possibilities leads us to conclude (1) that the discrepancy is larger than can be accounted for by assuming that the visible limb is lower than 110 km, and (2) that a positive bias of about 3 degrees added to the roll-angle data would map the limb to approximately the correct position. As Figure 5a shows, the estimated roll includes a suspicious -3 degree offset, thus reinforcing the evidence from the image data. (The roll estimated for PB2045, Figure 5b, includes a similar bias.) Rosenberg also has noticed this apparent discrepancy and has developed compensation techniques for data with discernible limbs [2].

It will be necessary to examine more data before definitive conclusions can be reached on the consistency of image and attitude data. It may be fruitful also to compare observed terminator geometries with their predicted form. Overlays of concurrent all-sky camera and AIRS images should provide additional information useful for assessing the geometric integrity of the restored images.

The severity of platform motions present in PB2045 makes the geometric restoration of those data a dubious proposition. We see in Plate 6 that the terminator is approximately "linearized". (This pass occurred close to the spring equinox, a time for which the terminator should pass through the pole and, hence, project onto our polar map as a straight line.) Given the complexity of shape of the raw terminator (see Plate 2), this aspect of the restoration is quite satisfying.

The yaw excursions in this pass produced large areas that were scanned more than once. The terminator should be approximately stationary over the twelve-minute pass duration, and the position discrepancies between the various terminator overscans in Plate 6 give some indication of the accuracy of the restoration processing for cases of extreme motion. In other regions of the image, particularly near

the limb when the yaw motion is most rapid, the scanner field of view moves so rapidly that successive scans do not overlap. Consequently, small-scale structures in these regions may be undersampled.

The restored images presented here show only the last pass over regions that were scanned more than once. Early observations in a given pass simply are covered up by later observations that happen to project to the same area. It is easy to modify the processing so that redundant pixels retain either the maximum value or, alternatively, the average value.



#### 4 Conclusions

We have developed software for the geometric restoration of AIRS image data. Our approach is based on rigorous geometric principles and is applicable to circumstances with arbitrary satellite position and attitude variations. No small-amplitude or slow-variation assumptions are made. For efficiency, the processing is in two steps: geometry calculations, and image projection. The first step creates a sorted interpolation table, which can be used efficiently to project several images.

The restoration software has been exercised on a small sample of the AIRS data. This processing has been performed both for performance assessments and to provide *ad hoc* support to other research efforts. For example, the image data relevant to the HIPASS experiment were processed, and specialized display formats were developed to enhance localized activity.

Our results indicate that useful geometrically restored images can be generated efficiently on a small computer. Because our approach can be used to project image data to any viewport on any map projection, it should be effective in correlative studies of data from multiple sensors. It is possible, for example, to display in one image concurrent AIRS passes from independent receivers, all-sky camera imagery, and other relevant spatial measurements, such as radar and beacon data and data from *in-situ* probes.

In general, the accuracy of image restoration will be limited by the accuracy of satellite attitude information. Our results demonstrate that the image data, particularly terminator and limb geometries, can be used to assess the consistency of the attitude data. We recommend that attitude estimation procedures be improved so that (1) the attitude estimates are as accurate as possible, (2) error bounds will be available for these data, and (3) attitude can be estimated even when the magnetometer and sun-sensor data are incomplete. This last will be useful both to fill in short gaps existing within certain passes and to provide night-side attitude estimates.

The preparation of multiple-image projections, for example with AIRS data from distinct receivers and concurrent all-sky images and other relevant data, is now possible. We recommend that the appropriate records and logs be surveyed to identify appropriate data for this purpose. Since all-sky images come only from the night side, we will need either (1) very stable Polar BEAR orientation so that nominal attitude can be assumed, or (2) instances where the satellite was in sunlight and transmitted image data concurrent with all sky imagery recorded in darkness, or (3) successful techniques for estimating satellite attitude on the night side.

## REFERENCES

- [1] LUCAS, R.D.; ROBINS, R.E. (1985) "Phase I Final Report: Implementation of an ionospheric-image file management, processing, and display system," Physical Dynamics Report PD-NW-85-331R (AFGL-TR-85-0082), 15 April 1985. ADA164502
- [2] ROSENBERG, N. (1987) "Satellite UV Image Processing," Technical Report NWRA-CR-87-R016, 9 October 1987.
- [3] FOLEY, J.D.; VAN DAM, A. (1982) Fundamentals of Interactive Computer Graphics, Addison Wesley, Reading.



Plate 1



Plate 2



Plate 3



Plate 4



Plate 5



Plate 6

END

DATE  
FILMED  
5-88

DTIC